Demonstration of neutron identification in neutrino interactions in the MicroBooNE liquid argon time projection chamber

P. Abratenko,[40] O. Alterkait,[40] D. Andrade Aldana,[15] L. Arellano,[22] J. Asaadi,[39] A. Ashkenazi,[37]
S. Balasubramanian,[12] B. Baller,[12] A. Barnard,[29] G. Barr,[29] D. Barrow,[29] J. Barrow,[26] V. Basque,[12] J. Bateman,[22]
O. Benevides Rodrigues,[15] S. Berkman,[25] A. Bhanderi,[22] A. Bhat,[7] M. Bhattacharya,[12] M. Bishai,[3] A. Blake,[19]
B. Bogart,[24] T. Bolton,[18] J. Y. Book,[14] M. B. Brunetti,[43] L. Camilleri,[10] Y. Cao,[22] D. Caratelli,[4] F. Cavanna,[12]
G. Cerati,[12] A. Chappell,[43] Y. Chen,[33] J. M. Conrad,[23] M. Convery,[33] L. Cooper-Troendle,[30] J. I. Crespo-Anadón,[6]
R. Cross,[43] M. Del Tutto,[12] S. R. Dennis,[5] P. Detje,[5] R. Diurba,[2] Z. Djurcic,[1] R. Dorrill,[15] K. Duffy,[29] S. Dytman,[30]
B. Eberly,[35] P. Englezos,[32] A. Ereditato,[7, 12] J. J. Evans,[22] R. Fine,[20] W. Foreman,[15] B. T. Fleming,[7] D. Franco,[7]
A. P. Furmanski,[26] F. Gao,[4] D. Garcia-Gamez,[13] S. Gardiner,[12] G. Ge,[10] S. Gollapinni,[20] E. Gramellini,[22]
P. Green,[29] H. Greenlee,[12] L. Gu,[19] W. Gu,[3] R. Guenette,[22] P. Guzowski,[22] L. Hagaman,[7] M. D. Handley,[5]
O. Hen,[23] C. Hilgenberg,[26] G. A. Horton-Smith,[18] Z. Imani,[40] B. Irwin,[26] M. S. Ismail,[30] C. James,[12] X. Ji,[27]
J. H. Jo,[3] R. A. Johnson,[8] Y.-J. Jwa,[10] D. Kalra,[10] N. Kamp,[23] G. Karagiorgi,[10] W. Ketchum,[12] M. Kirby,[3]
T. Kobilarcik,[12] I. Kreslo,[2] N. Lane,[22] J.-Y. Li,[11] Y. Li,[3] K. Lin,[32] B. R. Littlejohn,[15] H. Liu,[3] W. C. Louis,[20]
X. Luo,[4] C. Mariani,[42] D. Marsden,[22] J. Marshall,[43] N. Martinez,[18] D. A. Martinez Caicedo,[34] S. Martynenko,[3]
A. Mastbaum,[32] I. Mawby,[19] N. McConkey,[31] V. Meddage,[18] J. Mendez,[21] J. Micallef,[23, 40] K. Miller,[7] A. Mogan,[9]
T. Mohayai,[17] M. Mooney,[9] A. F. Moor,[5] C. D. Moore,[12] L. Mora Lepin,[22] M. M. Moudgalya,[22] S. Mulleriababu,[2]
D. Naples,[30] A. Navrer-Agasson,[16, 22] N. Nayak,[3] M. Nebot-Guinot,[11] C. Nguyen,[32] J. Nowak,[19] N. Oza,[10]
O. Palamara,[12] N. Pallat,[26] V. Paolone,[30] A. Papadopoulou,[1] V. Papavassiliou,[28] H. B. Parkinson,[11] S. F. Pate,[28]
N. Patel,[19] Z. Pavlovic,[12] E. Piasetzky,[37] K. Pletcher,[25] I. Pophale,[19] X. Qian,[3] J. L. Raaf,[12] V. Radeka,[3]
A. Rafique,[1] M. Reggiani-Guzzo,[11] L. Ren,[28] L. Rochester,[33] J. Rodriguez Rondon,[34] M. Rosenberg,[40]
M. Ross-Lonergan,[20] I. Safa,[10] D. W. Schmitz,[7] A. Schukraft,[12] W. Seligman,[10] M. H. Shaevitz,[10]
R. Sharankova,[12] J. Shi,[5] E. L. Snider,[12] M. Soderberg,[36] S. Söldner-Rembold,[16, 22] J. Spitz,[24] M. Stancari,[12]
J. St. John,[12] T. Strauss,[12] A. M. Szelc,[11] W. Tang,[38] N. Taniuchi,[5] K. Terao,[33] C. Thorpe,[22] D. Torbunov,[3]
D. Totani,[4] M. Toups,[12] A. Trettin,[22] Y.-T. Tsai,[33] J. Tyler,[18] M. A. Uchida,[5] T. Usher,[33] B. Viren,[3]
J. Wang,[27] M. Weber,[2] H. Wei,[21] A. J. White,[7] S. Wolbers,[12] T. Wongjirad,[40] M. Wospakrik,[12] K. Wresilo,[5]
W. Wu,[30] E. Yandel,[4] T. Yang,[12] L. E. Yates,[12] H. W. Yu,[3] G. P. Zeller,[12] J. Zennamo,[12] and C. Zhang[3]

(The MicroBooNE Collaboration)*

[1] *Argonne National Laboratory (ANL), Lemont, IL, 60439, USA*
[2] *Universität Bern, Bern CH-3012, Switzerland*
[3] *Brookhaven National Laboratory (BNL), Upton, NY, 11973, USA*
[4] *University of California, Santa Barbara, CA, 93106, USA*
[5] *University of Cambridge, Cambridge CB3 0HE, United Kingdom*
[6] *Centro de Investigaciones Energéticas, Medioambientales y Tecnológicas (CIEMAT), Madrid E-28040, Spain*
[7] *University of Chicago, Chicago, IL, 60637, USA*
[8] *University of Cincinnati, Cincinnati, OH, 45221, USA*
[9] *Colorado State University, Fort Collins, CO, 80523, USA*
[10] *Columbia University, New York, NY, 10027, USA*
[11] *University of Edinburgh, Edinburgh EH9 3FD, United Kingdom*
[12] *Fermi National Accelerator Laboratory (FNAL), Batavia, IL 60510, USA*
[13] *Universidad de Granada, Granada E-18071, Spain*
[14] *Harvard University, Cambridge, MA 02138, USA*
[15] *Illinois Institute of Technology (IIT), Chicago, IL 60616, USA*
[16] *Imperial College London, London SW7 2AZ, United Kingdom*
[17] *Indiana University, Bloomington, IN 47405, USA*
[18] *Kansas State University (KSU), Manhattan, KS, 66506, USA*
[19] *Lancaster University, Lancaster LA1 4YW, United Kingdom*
[20] *Los Alamos National Laboratory (LANL), Los Alamos, NM, 87545, USA*
[21] *Louisiana State University, Baton Rouge, LA, 70803, USA*
[22] *The University of Manchester, Manchester M13 9PL, United Kingdom*
[23] *Massachusetts Institute of Technology (MIT), Cambridge, MA, 02139, USA*
[24] *University of Michigan, Ann Arbor, MI, 48109, USA*
[25] *Michigan State University, East Lansing, MI 48824, USA*
[26] *University of Minnesota, Minneapolis, MN, 55455, USA*
[27] *Nankai University, Nankai District, Tianjin 300071, China*
[28] *New Mexico State University (NMSU), Las Cruces, NM, 88003, USA*
[29] *University of Oxford, Oxford OX1 3RH, United Kingdom*

[30]*University of Pittsburgh, Pittsburgh, PA, 15260, USA*
[31]*Queen Mary University of London, London E1 4NS, United Kingdom*
[32]*Rutgers University, Piscataway, NJ, 08854, USA*
[33]*SLAC National Accelerator Laboratory, Menlo Park, CA, 94025, USA*
[34]*South Dakota School of Mines and Technology (SDSMT), Rapid City, SD, 57701, USA*
[35]*University of Southern Maine, Portland, ME, 04104, USA*
[36]*Syracuse University, Syracuse, NY, 13244, USA*
[37]*Tel Aviv University, Tel Aviv, Israel, 69978*
[38]*University of Tennessee, Knoxville, TN, 37996, USA*
[39]*University of Texas, Arlington, TX, 76019, USA*
[40]*Tufts University, Medford, MA, 02155, USA*
[41]*University College London, London WC1E 6BT, United Kingdom*
[42]*Center for Neutrino Physics, Virginia Tech, Blacksburg, VA, 24061, USA*
[43]*University of Warwick, Coventry CV4 7AL, United Kingdom*
(Dated: August 2, 2024)

A significant challenge in measurements of neutrino oscillations is reconstructing the incoming neutrino energies. While modern fully-active tracking calorimeters such as liquid argon time projection chambers in principle allow the measurement of all final state particles above some detection threshold, undetected neutrons remain a considerable source of missing energy with little to no data constraining their production rates and kinematics. We present the first demonstration of tagging neutrino-induced neutrons in liquid argon time projection chambers using secondary protons emitted from neutron-argon interactions in the MicroBooNE detector. We describe the method developed to identify neutrino-induced neutrons and demonstrate its performance using neutrons produced in muon-neutrino charged current interactions. The method is validated using a small subset of MicroBooNE's total dataset. The selection yields a sample with 60% of selected tracks corresponding to neutron-induced secondary protons. At this purity, the integrated efficiency is 8.4% for neutrons that produce a detectable proton.

I. INTRODUCTION

With the study of neutrino oscillations moving into a precision measurement era with the Deep Underground Neutrino Experiment (DUNE) and Hyper-Kamiokande (Hyper-K) experiments under construction [1, 2], significant work is still needed to reduce the uncertainties that arise due to the modeling of neutrino-nucleus interactions. As neutrino energies are typically estimated based on the visible final state particles produced in their interactions (e.g. [3–5]), the presence of neutrons will bias these estimates even for fully active detectors such as the liquid argon time projection chamber (LArTPC) technology that DUNE will use. While developments have been made in understanding and improving neutrino energy resolutions using new methods [6–8], neutrons will always represent a bias that requires model-dependent corrections. To first order, the neutrino's reconstructed energy will be biased by the full kinetic energy of the neutron. While neutrons produced in neutrino interactions can be observed through capture processes, particularly in gadolinium-loaded detectors [9, 10], this technique is not easily applicable to LArTPC detectors. Neutrino-induced neutrons can also be measured through inelastic scatters with nuclei, for example using liquid scintillator detectors (as demonstrated by the COHERENT experiment [11]) or in solid scintillator detectors (e.g. in the

MINERvA experiment [12, 13]). In the case of the MINERvA experiment, these measurements were made using antineutrino interactions which tend to produce more neutrons. It has also been shown using the ArgoNeuT detector that neutrons can be identified in a LArTPC through the photons produced by the de-excitations of excited argon nuclei produced in neutron inelastic scatters [14]. This work introduces a method of identifying neutrino-induced neutrons in a liquid argon TPC using neutron-argon inelastic scatters that produce a secondary proton, similar to the technique demonstrated by MINERvA. The method is validated using data from the MicroBooNE detector.

A. MicroBooNE Detector

The MicroBooNE LArTPC detector is a $2.56\,(x) \times 2.33\,(y) \times 10.37\,(z)\,\mathrm{m}^3$, 85 tonne active volume LArTPC exposed to the Booster Neutrino Beam (BNB) at Fermi National Accelerator Laboratory that took data between 2015-2021, with an exposure of 1.49×10^{21} protons on target (POT) [15]. This work uses a subset of that data, corresponding to an exposure of 4.13×10^{19} POT delivered in 2017-2018. The MicroBooNE detector is located 468 m downstream of the target, at which point the neutrino beam primarily consists of ν_μ (93.7%) with a mean energy of $\sim 800\,\mathrm{MeV}$ [16]. Charged particles produced in neutrino-argon interactions propagate through the LArTPC and ionize the argon atoms. The ionized charge drifts in a 273 V/cm

electric field towards the anode that consists of two induction planes and one collection plane, with 3 mm pitch between wires and 3 mm plane separation [17]. The full drift time for an electron in MicroBooNE is 2.3 ms. There is an average of six cosmogenic particles in the detector during a drift window [18, 19]. The LArTPC is paired with 32 photo-multiplier tubes (PMTs) that identify scintillation photons from argon atoms excited by particles traversing the liquid argon. By leveraging the time and spatial structure of the scintillation light, and comparing to the visible TPC activity, cosmogenic backgrounds that are out of time with the 1.6 μs BNB spill can be efficiently tagged and removed.

B. MicroBooNE Simulation

The MicroBooNE collaboration uses software that employs a series of Monte Carlo simulations that model all aspects of the experiment. The BNB flux simulation was originally developed by the MiniBooNE collaboration [16] and then customized for MicroBooNE. The neutrino-argon interactions are modeled in the MicroBooNE simulation chain using the GENIE v3.0.6 neutrino event generator [20, 21] with a modified version of the G18_10a_02_11a tune. This modified tune of G18_10a_02_11a was developed to better fit the 2016 CC0π T2K dataset [22]. Final state particles from the interactions simulated by GENIE are propagated through the MicroBooNE detector using GEANTv4_10_3_p03c [23, 24]. The physics package used in the MicroBooNE version of GEANT4 is the quark-gluon string model and the Bertini cascade model (QGSP_BERT) [23]. Data taken while the BNB is off is overlaid on the simulated neutrino interaction to describe both the cosmic background and intrinsic detector noise. The detector response is modeled in the LArSoft framework [25].

The neutrons of interest in this work are produced in neutrino interactions. An additional source of neutrons comes from secondary interactions of neutrino-induced hadrons within the detector volume. These neutrons are distinct from the primary neutrons in that they originate from a different nucleus. However, their signatures are indistinguishable and they constitute an irreducible background to primary neutrons from the neutrino interaction.

II. NEUTRON DETECTION

In order to tag and identify neutrons in neutrino interactions on argon, it is important to understand their behavior as they propagate through the detector. This section outlines the characteristics of neutron inelastic scattering on argon.

Tables I- III summarize the behavior of neutrons in the MicroBooNE detector, according to the GEANT4 simulation deployed. Importantly, of the neutrons in our sample, 71.45% inelastically scatter at least once within the detector before leaving the active volume. The majority of neutrons inelastically scatter only once (30.28%) or twice (26.51%). More than half (54.13%) of neutron inelastic scatters result in only the original neutron and the possibly excited secondary argon atom, while another 30.86% of scatters produce additional neutrons. Finally, 8.85% of neutron-argon inelastic scatters create protons, with 6.60% of scatters including one proton and 1.37% of scatters including two protons.

For BNB neutrino-induced neutrons in MicroBooNE, the flux-integrated cross section is dominated by the 1 neutron and 2 or more neutron final states, due to the low average neutron energies. Figure 1 shows the neutron-argon inelastic scattering cross section (as extracted from the GEANT4 simulation) as a function of the neutron kinetic energy and broken down by the final states listed in Table III. The cross section is only shown for neutron energies above 40 MeV, the rough minimum to which our analysis method – reconstruction of a secondary proton track – is sensitive. The energy spectrum predicted by the GENIE simulation for neutrons produced by neutrinos in MicroBooNE is shown in gray, with arbitrary normalization. These theoretical predictions have not been directly validated with data [26], although in the energy range of interest the total (including elastic interactions) neutron-argon cross section has been measured [27]. The neutron-argon total cross section between neutron kinetic energies of 95 and 720 MeV is fairly flat and approximately 700 mb, corresponding to a mean free path in liquid argon of ∼70 cm.

In the energy range of interest (between 40 and 600 MeV), the proton production cross section is approximately flat. The detection method presented here targets secondary protons produced by inelastic scatters, represented by the pink and blue lines in Fig 1. Proton-generating processes become the dominant predicted exclusive interaction channel above roughly 300 MeV in neutron kinetic energy. A similar method has been shown to work to identify neutrons in the ProtoDUNE detector [28].

TABLE I: Final state neutron end processes for simulated neutrino-induced primary neutrons.

Neutron End Process	
Exit detector without inelastic scatter	24.63%
Exit detector after inelastic scatter	71.45%
Captured by argon	3.13%
Other	0.75%

The most frequent type of neutron interaction leaves the argon nucleus in an excited state without producing another visible signature. In principle, MicroBooNE has the LArTPC detector response attributes and existing low-energy reconstruction tools [29, 30] to tag neutrons through de-excitation photons. While previous demonstrations of identifying such events have been produced
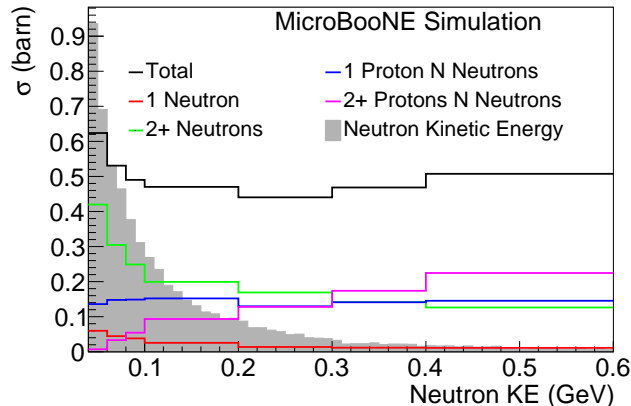
FIG. 1: Neutron-argon inelastic scattering cross section as a function of neutron kinetic energy and broken down by the most common inelastic scatter final states. The predicted neutron energy spectrum is shown in gray, with arbitrary normalization.
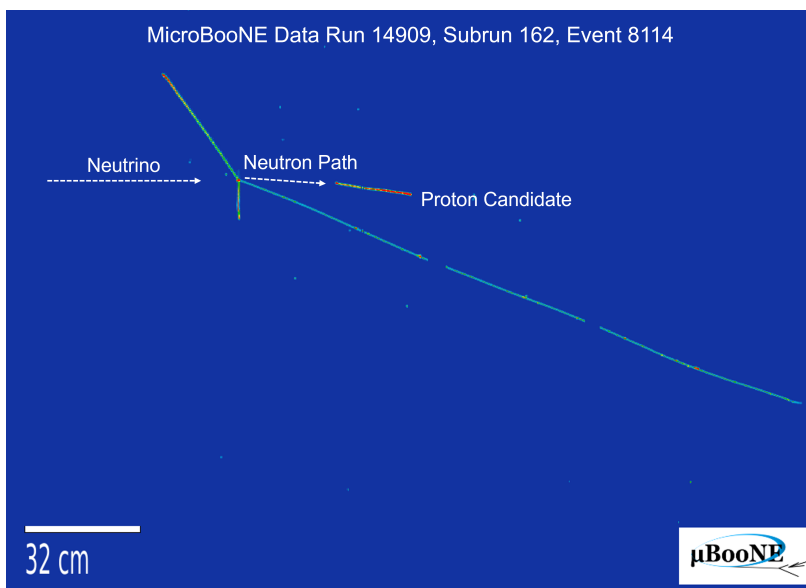

FIG. 2: Data event showing ν_μ CC candidate with a final state neutron candidate. A secondary proton track candidate is seen in the middle of the image. Image is of the collection plane. Here the horizontal axis shows the z direction and the vertical axis shows the x direction in the MicroBooNE detector. Charge deposited is represented by the color scale, where blue corresponds to small charge deposits and red corresponds to large charge deposits.

[14], these interactions present unique challenges that complicate their application to the problem of neutrino calorimetry [31]. When leveraging low energy photons, there is a contaminating population of photons from de-excitation of the remnant nucleus from the initial neutrino interaction, as well as a large amount of cosmogenic and radiogenic low energy EM activity, especially in a surface LArTPC such as the MicroBooNE detector. In addition, the isotropic nature of these de-excitation photons, along with a 14 cm radiation length in LAr, means any directional information which could help constrain the neutron's kinematics is significantly smeared

[14, 32]. The detection method presented here targets instead the secondary protons produced by inelastic scatters. While this interaction mode is less common, these events present fewer problematic backgrounds, and the secondary proton location can be used to better estimate the neutron direction. Additionally, higher energy protons are produced more frequently by higher energy neutrons which are the most relevant when considering potential biases to neutrino energy estimation.

It is worth noting that the number of neutrons that produce visible protons depends on the detector geometry. With the MicroBooNE detector being less than 2.5
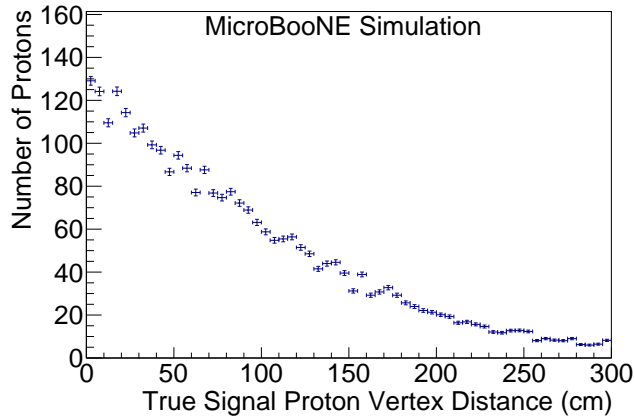
FIG. 3: Neutrino vertex displacement for true secondary protons created from final state neutrons. Error bars shown here only represent statistical error.
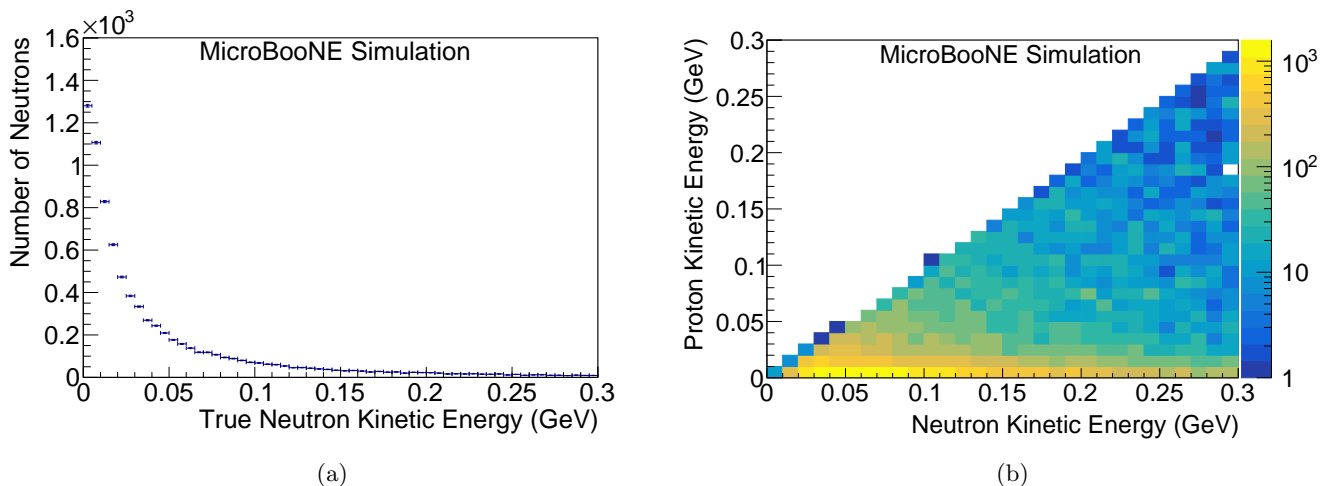

(a)

(b)

FIG. 4: (a) Kinetic energy spectrum for all ν_μ CC final state true neutrons. (b) Correlation between parent neutron kinetic energy and daughter proton kinetic energy made from MicroBooNE simulation. Error bars shown here only represent statistical error.

TABLE II: Number of times neutrino-induced primary neutrons inelastically scatter.

Number of Inelastic Scatters	
0 scatters	25.48%
1 scatter	30.28%
2 scatters	26.51%
3 scatters	11.87%
4+ scatters	5.87%

m in dimensions of width and height, all neutrino interactions are less than 2 neutron interaction lengths from the nearest detector boundary. A larger detector, such as those being constructed for DUNE, will therefore have a higher efficiency for tagging neutrons.

TABLE III: Final state particles of neutron-argon inelastic scatters for simulated neutrino-induced primary neutrons

Final State of Scatter	
(1) Ar*	54.13%
(2) Ar* $+ Nn$	30.86%
(3) Cl $+ Nn + 1p$	6.60%
(4) S $+ Nn + 2p$	1.37%
(5) S $+ Nn + \alpha$	2.14%
(6) Other proton final state	0.88%
(7) Other	4.03%

Figure 2 shows a MicroBooNE data event display that includes a charged current (CC) candidate interaction
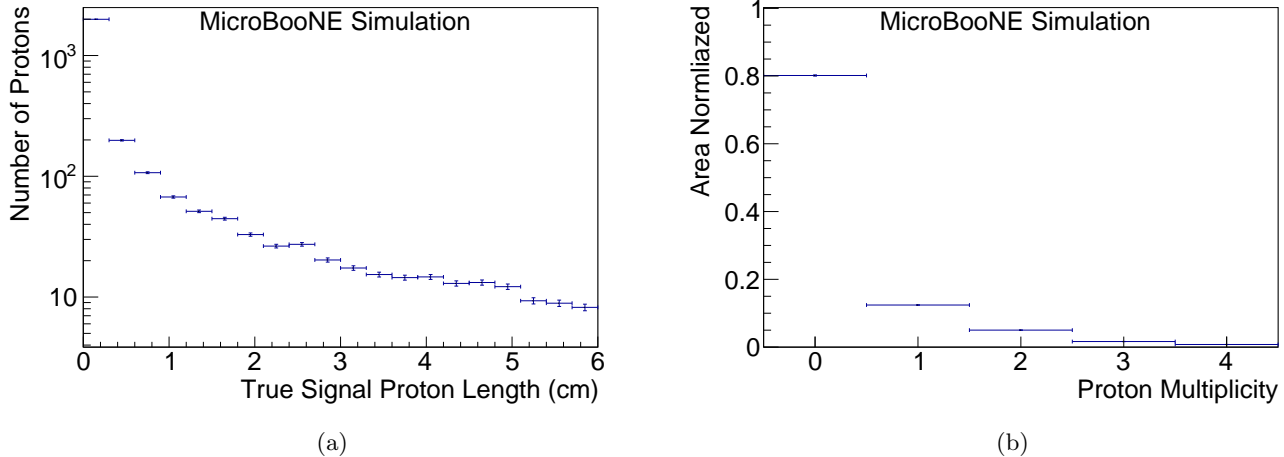
FIG. 5: (a) Track length of true secondary protons created from final state neutrons. (b) Area normalized number of protons produced by final state neutrons. Error bars shown here only represent statistical error.

(upper left of image) with a final state neutron candidate. This neutron re-scatters on an argon nucleus and produces the proton track candidate (red track in the center of the image). Position information from this track allows for the reconstruction of the direction of the neutron, as well as the distance between the secondary proton and the neutrino interaction vertex.

Identifying neutrons via secondary protons presents certain challenges. The falling distribution in Fig. 3 shows that many secondary protons appear distant from the true neutrino vertex. Most neutrons produced in neutrino interactions from the BNB are very low energy (Fig. 4a) and because neutrons transfer a small amount of kinetic energy to the daughter protons, there is minimal correlation between the neutron's kinetic energy and the secondary proton's kinetic energy (Fig. 4b). This results in short proton tracks which are hard to identify. Figure 5a shows the true secondary proton track length distribution from simulation. The majority of the protons ($\sim$74%) created from final state neutrons travel less than 3 mm, meaning that they can cross at most 1 wire from a single plane in the detector. Figure 5b shows the number of protons produced by a final state neutron, showing that 70% of neutrons do not produce any secondary protons at all. While Table III suggests that only around 8% of scatters produce a proton, neutrons can scatter multiple times providing more opportunities to produce a proton from any individual neutron. Though this identification method leads to a very low efficiency for low energy neutrons, it does identify higher-energy neutrons at a higher efficiency.

III.   EVENT SELECTION

The reconstruction of charged particle tracks is performed by the Pandora multi-algorithm pattern recogni-

tion toolkit [33] which we briefly describe here. Hits on the three planes are passed to the Pandora cosmic reconstruction to first identify unambiguous cosmic-ray muons and their daughter delta rays. Hits associated with these backgrounds are removed from the input hit collection. This hit collection is subsequently passed to the Pandora neutrino reconstruction. Some cosmic tracks—the ones that are not obviously of cosmic origin—are deliberately reconsidered in the next stage of the reconstruction to avoid possible loss of neutrino-induced tracks at an early stage in the process. The remaining hits are divided into groups, called slices, that Pandora classifies as related using proximity and direction-based metrics with the goal of isolating the various interactions in the detector, whether induced by a neutrino or cosmic-ray. Cosmic-ray-oriented and neutrino-oriented clustering and topological algorithms are separately applied to the hits in each slice, so that the two outcomes can be compared. The most appropriate outcome is identified for each slice. Collections of hits within each slice are reconstructed to form particle flow particles (PFPs)— a general term that can refer to either a shower or a track—and a topological score is calculated for each slice using a support vector machine (SVM). Slices resembling a neutrino interaction get a score closer to 1 and slices resembling cosmic activity get a score closer to 0. Based on this score and confirming that the candidate neutrino slice has a flash that is in time with the BNB spill, at most one neutrino slice candidate per event is chosen. The slicing process is especially relevant for the reconstruction of neutrons, since they regularly scatter far away from the neutrino vertex and daughter protons are often not included in the neutrino slice.

We begin our preselection with the sample of events identified as ν_μ CC as in [34] where the neutrino vertex is contained in the fiducial volume:

$$21.50\,\text{cm} \leq x \leq 234.85\,\text{cm},$$
$$\text{-95.00}\,\text{cm} \leq y \leq 95.00\,\text{cm},$$
$$21.50\,\text{cm} \leq z \leq 966.80\,\text{cm}.$$

We additionally require all candidate tracks to be fully contained in a "containment volume" [34]:

$$10.00\,\text{cm} \leq \text{x} \leq 246.35\,\text{cm},$$
$$\text{-106.50}\,\text{cm} \leq \text{y} \leq 106.50\,\text{cm},$$
$$10.00\,\text{cm} \leq \text{z} \leq 1026.80\,\text{cm}.$$

We then consider all reconstructed PFPs within the neutrino slice to search for secondary protons from primary neutrons. For the purpose of studying the selection's performance, we group these into a variety of categories based on their origin:

1. Signal Proton: Track belongs to a secondary proton produced by a final state neutron through neutron-inelastic scatter (final states (3), (4), and (6) in Tab. III).

2. Neutron Inelastic (NI) Proton (non-signal): Track belongs to a tertiary proton that has been produced by a neutrino-generated, non-final state neutron through neutron-inelastic scatter (final states (3), (4), and (6) in Tab. III).

3. Primary Particle: Track belongs to a final state particle produced directly in the neutrino interaction.

4. Proton Inelastic (PI) Proton: Track belongs to a secondary proton produced through proton-inelastic scatter.

5. Other Particle: Track belongs to any other simulated particle.

6. Dirt: Track originates from a neutrino interaction that occurred in the detector hall or dirt surrounding the detector complex.

7. Cosmics and MC EM: Track belongs to either simulated electromagnetic (EM) activity or data cosmic activity overlaid on top of simulated neutrino event.

8. BNB Beam-Off Data: Cosmic-induced backgrounds, measured with data taken when the beam was off.

9. BNB Beam-On Data.

All figures showing MicroBooNE simulation have been normalized to the data sample exposure used in this study (4.13×10^{19} POT). BNB Beam-Off Data has been normalized to the total number of triggers in the BNB Beam-On Data sample. We define the integrated efficiency of the selection as the ratio between the number of true neutrons tagged from daughter proton tracks to the total number of true final state neutrons in the MC sample. The selection purity is defined as the ratio of the number of signal proton tracks to the number of selected candidate tracks. NI non-signal protons are a background of particular interest. Neutrino-generated neutrons that are created from the inelastic, secondary scatters of final state hadrons (primarily protons and pions) with argon nuclei can then scatter again and create tertiary protons. Although this background is effectively indistinguishable from our signal, identifying these neutrons is still useful. The presence of any neutrino-generated neutrons indicates that there is missing energy, biasing the neutrino energy reconstruction. Therefore, we will also report the NI produced proton purity, defined here as the ratio of the number of signal and NI proton tracks to the number of selected candidate tracks.

We require that neutron induced proton track candidates be reconstructed as part of the neutrino interaction by Pandora. While this requirement rejects the majority (62.0%) of our signal, it helps reject 95.6% of our background. This information is shown in Fig. 6, where the large background rejection achieved by discarding tracks not reconstructed as part of the interaction ("Not in ν slice") can be seen. Future iterations of the analysis will attempt to recover these protons.

Once PFPs that are not included in the neutrino slice are eliminated, the leading backgrounds are primary, BNB Beam-Off, Cosmic/EM MC tracks, and PI protons (Fig. 7). The primary and PI proton backgrounds are both susceptible to uncertainties on GEANT4 modeling of particle propagation and reinteraction in the LAr. The MC EM background is sensitive to uncertainties from our particle identification which relies on dE/dx measurements. The dominant uncertainty on this is from electron-ion recombination [35].

At this point, both the Cosmic and BNB Beam-Off backgrounds are predominantly either muons or EM showers from muons. In order to eliminate them, we leverage two reconstruction variables. The first variable is the track/shower score, which is the output of an SVM in Pandora that determines if the PFP appears more track-like or shower-like (Fig. 7a). Tracks have scores closer to 1, while showers have scores closer to 0. The second reconstruction variable is the log-likelihood ratio particle identification (LLR PID) score (Fig. 7b) and is calculated using MicroBooNE-specific software that runs after Pandora completes its general reconstruction [36]. The score identifies tracks as more muon-like (closer to 1) or more proton-like (closer to -1). Both scores have been extensively vetted using MicroBooNE data and have been shown to be minimally impacted by systematic uncertainties [34, 37].

We remove most primary tracks by measuring the displacement between the candidate start point and the reconstructed neutrino vertex (Fig. 7c). After correcting for electric field distortions in our calibrations [17], both this variable and the proton candidate track length (Fig. 7d) are minimally impacted by the space charge
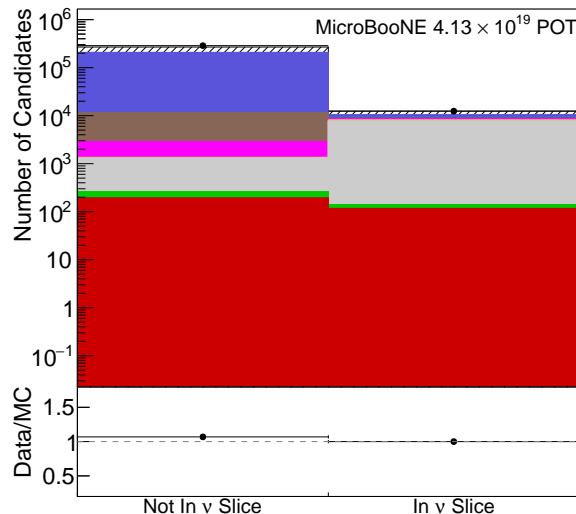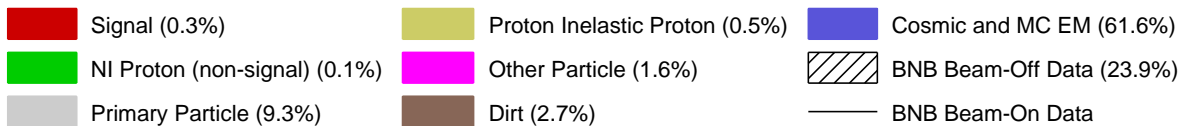
FIG. 6: Neutrino slice status for all fully contained tracks in ν_μ CC events. Error bars shown on MicroBooNE data represent only statistical uncertainty.

effect, with the largest effect when either the neutrino vertex or neutron candidate are close to the edge of the TPC.

The cuts on track/shower score, LLR PID score, and reconstructed vertex separation were optimized to maximize the product of the integrated neutron detection efficiency and signal purity. The selection criteria are:

- track/shower score > 0.1 (Fig. 7a),

- LLR PID score < -0.15 (Fig. 7b),

- vertex separation $10 < d < 200\,\mathrm{cm}$ (Fig. 7c).

The vertex separation and track length are shown in Fig. 8a and Fig. 8b for the surviving tracks. At this point, the largest backgrounds are proton-inelastic and primary protons. Unlike their neutron counterpart, the initiating proton in proton-inelastic tracks is visible in the detector. The secondary proton in proton inelastic interactions will inherently be in close proximity to the parent proton, thereby differentiating it from our signal. Assuming no nearby cosmic or primary PFPs, neutron produced proton tracks are isolated in space. We measure the shortest distance between either end of the secondary proton candidate, and the start and end points of every other PFP in the detector. The minimum of the 4N calculations—with N+1 being the number of PFPs in the detector including the current proton candidate—is the nearest PFP proximity. The variable "candidate

proximity to the nearest PFP" gives good discriminating power between signal and these two proton backgrounds and is shown in Fig. 8c.

Assuming the neutron direction is given by a straight line from the reconstructed neutrino vertex and the start of the proton candidate, we measure the cosine of the relative angle $(\cos(\chi))$ between the neutron direction and the candidate proton direction as seen in Fig. 8d. The candidate direction is defined as the vector between the reconstructed start and end positions of the candidate track. At this point in the event selection, the remaining cosmic, BNB Beam-Off, and Dirt tracks are likely neutron-induced protons. Neutrino-generated tracks should be forward-peaked in this variable due to momentum conservation whereas the other backgrounds should not. As the relative direction is specifically designed to reduce the neutron background that enters from outside the detector, it is particularly susceptible to the uncertainty on modeling neutrino interactions in the dirt around the detector [38]. However, the overall effect of dirt uncertainties should be small as the dirt background is very small. The selection criteria for both of the physics variables are:

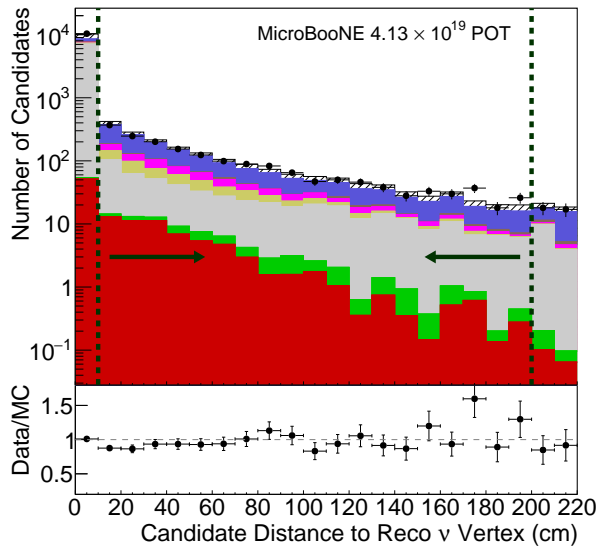- candidate PFP proximity $> 21\,\mathrm{cm}$,

- candidate track $\cos\chi > 0.2$.
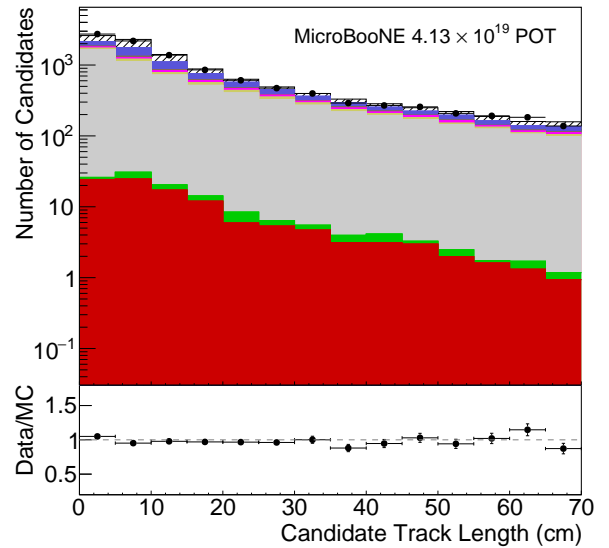
Both the PFP proximity and relative direction will also
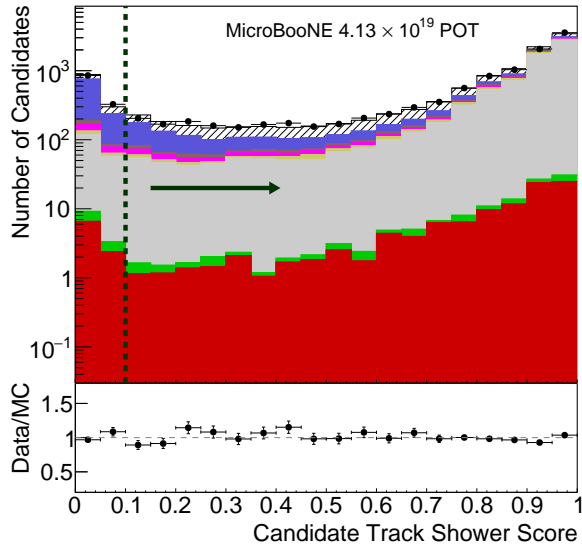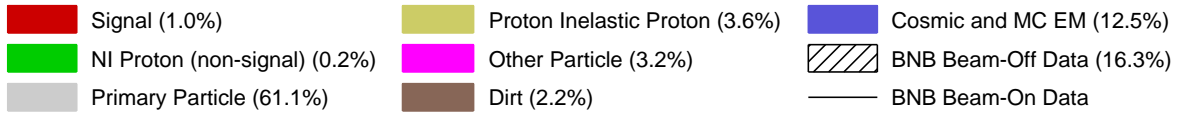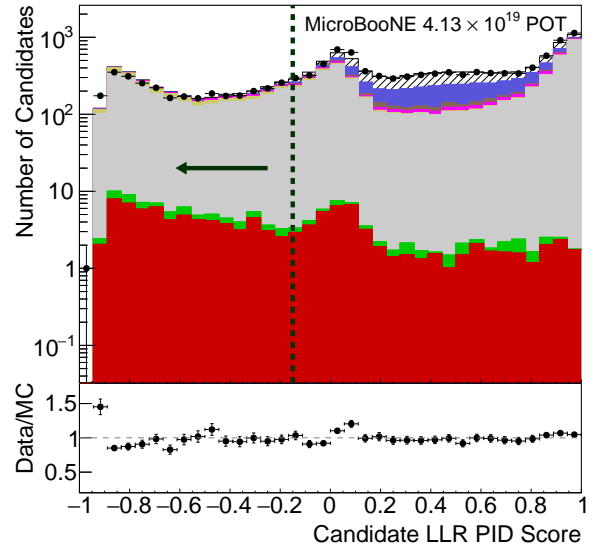
FIG. 7: All fully contained tracks in ν_μ CC events that are reconstructed in the neutrino slice. (a) track/shower SVM score, (b) LLR PID score, (c) displacement between the candidate and the reconstructed neutrino vertex, (d) candidate track length.
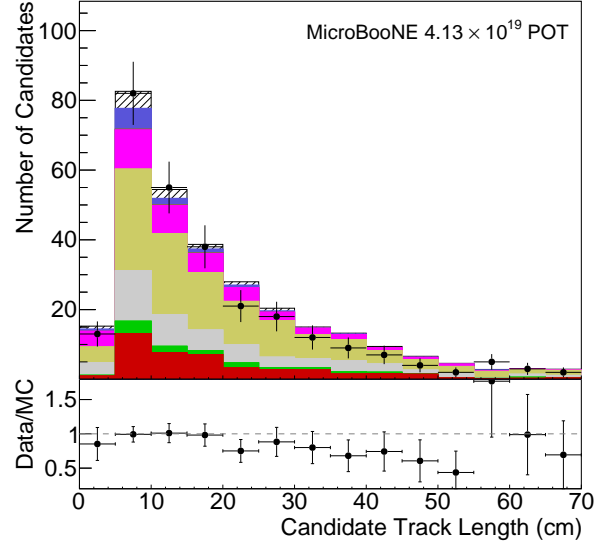
be minimally affected by the space charge effect in LArT-PCs.
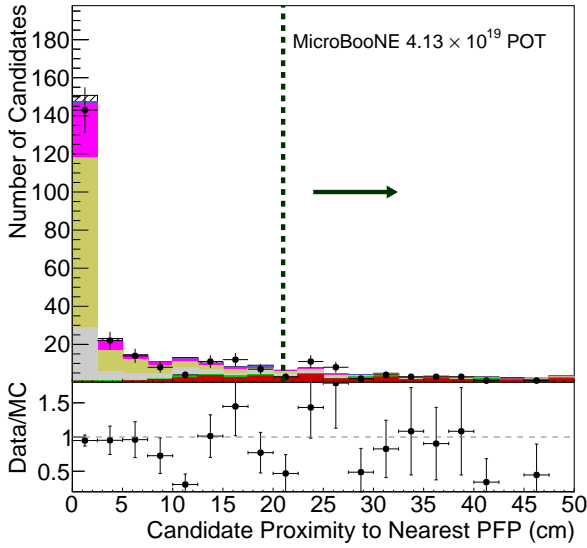
IV. EVENT SELECTION PERFORMANCE

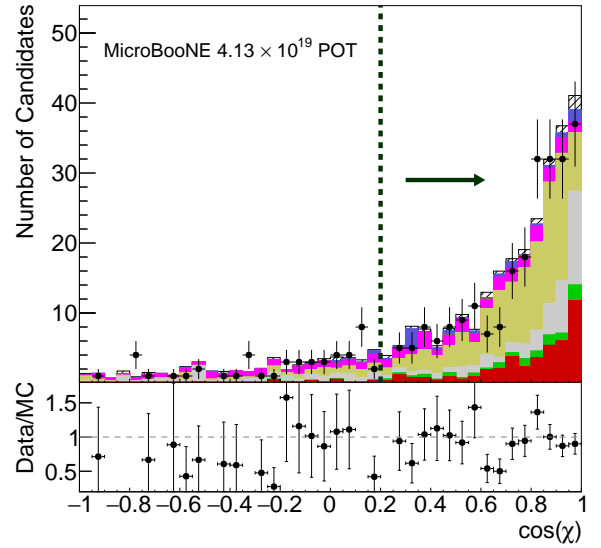The reconstructed neutrino vertex displacement and track length for the final set of neutron-generated, sec-
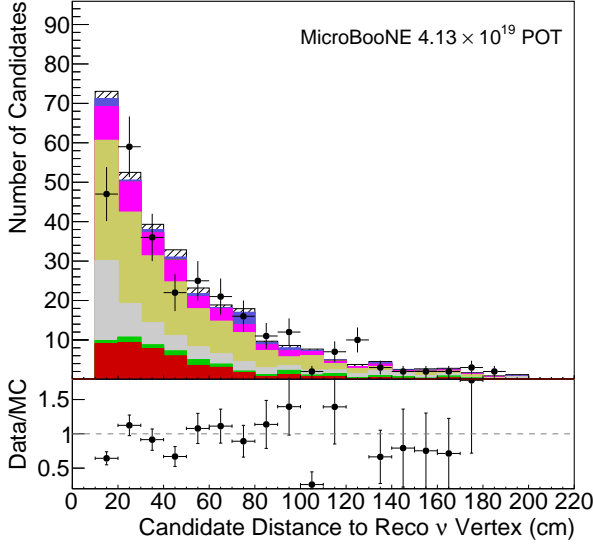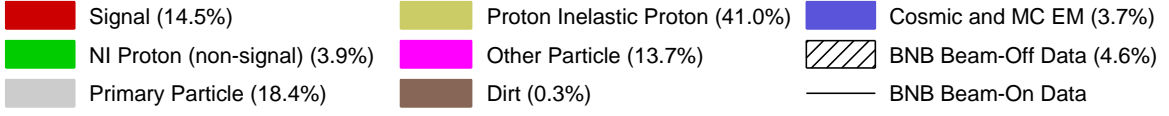
FIG. 8: Fully contained, neutrino-slice tracks in ν_μ CC events with LLR PID Score < -0.15, track/shower score > 0.1, and that lie between 10 and 200 cm of the reconstructed neutrino vertex. (a) Candidate displacement from the reconstructed neutrino vertex, (b) candidate track length, (c) Candidate proximity to nearest PFP, (d) and PFP relative direction or $\cos(\chi)$.

ondary proton track candidates is shown in Fig. 9a and 9b. These distributions demonstrate that the mod-

eling of neutron inelastic scatters in MicroBooNE agrees with data within the sizeable statistical uncertainties in
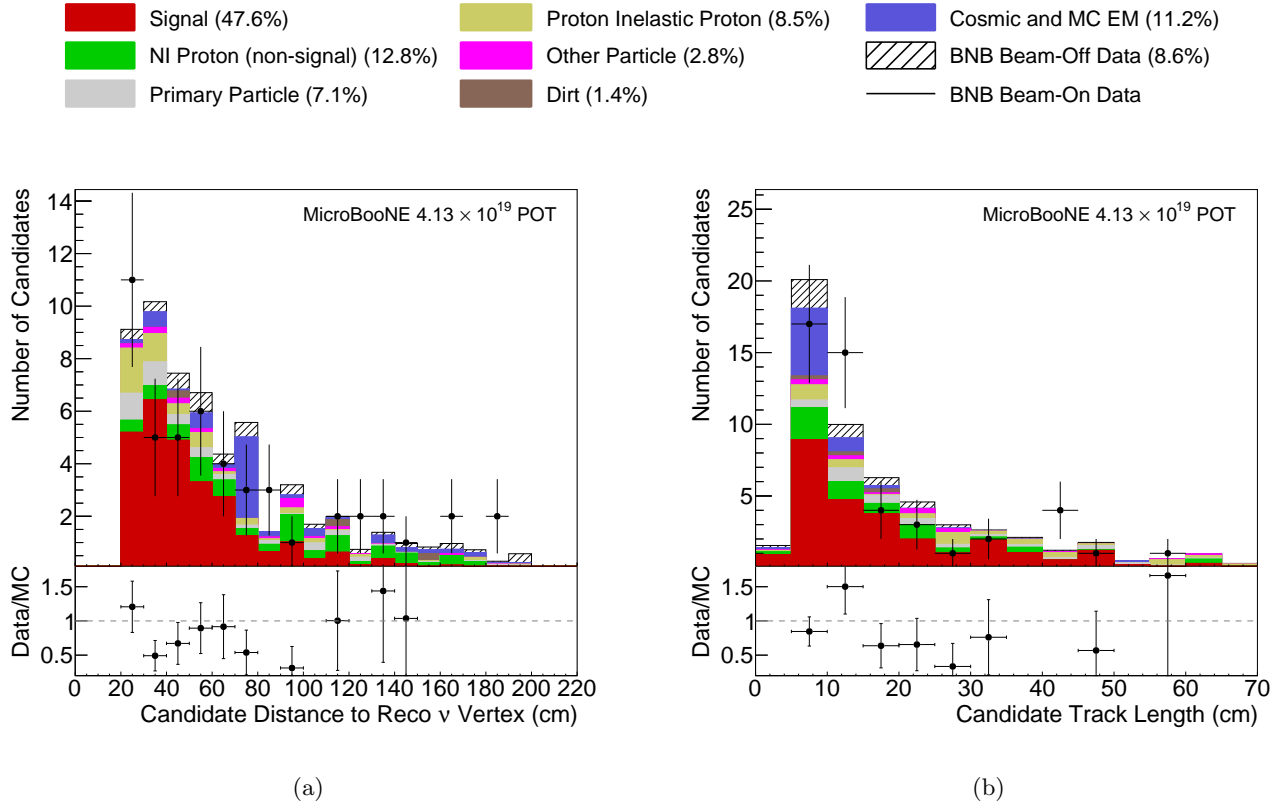
FIG. 9: (a) Final candidate displacement from the reconstructed neutrino vertex. (b) Final candidate track length.

this sample.

The final sample of neutron candidates is 48% pure primary neutrons, and 60% pure neutrino-induced neutrons (including non-signal neutrons), with the largest non-neutron backgrounds being cosmic particles, proton-inelastic protons, and primary particles (also primarily protons). Due to our use of data overlays to simulate background in the MC samples, it is not possible to know exactly what type of cosmic particles are being selected, but some fraction will be cosmogenic neutrons scattering close to the neutrino interaction.

Figure 10a shows the neutron detection efficiency as a function of true neutron kinetic energy at different stages in the event selection (error bars in Fig. 10 represent only statistical uncertainty). The final efficiency is negligible below neutron energies of around 100 MeV, rising to an approximately flat efficiency of around 3% above 250 MeV. The secondary proton detection efficiency as a function of true proton kinetic energy (Fig. 10b) shows that a significant source of inefficiency is failing to reconstruct and select protons below 50 MeV kinetic energy. This efficiency measures the detection rate of neutron-inelastically produced protons that start in the TPC. There are a small number of neutrons that create multiple secondary proton tracks that pass all event selection cuts. These neutrons are counted once when determining the neutron efficiency, however Fig. 10b counts each secondary proton independently. Due to this proton thresh-

old, we report an additional neutron detection efficiency as a function of neutron kinetic energy for neutrons that create a proton in the TPC with more than 50 MeV of true kinetic energy in Fig. 10c. Lastly, we report the neutron detection efficiency as a function of neutron polar scattering angle (defined as the angle from the beam direction) which shows better detection efficiency for neutrons that are more forward going (Fig. 10d). This higher detection efficiency at low polar angle is due to several reasons: forward-going neutrons tend to have higher energies leading to higher efficiency; the detector geometry means forward-going neutrons have a lower chance of exiting the detector before scattering; and the slicing performed by Pandora has some dependence on direction, therefore forward-going tracks are more likely to be classified as neutrino-like.

While the efficiency integrated across all neutron energies is low, the majority of neutrons produced are very low energy. For neutrons that create protons in the TPC with 50 MeV of kinetic energy or more, the integrated efficiency is 8.4%.

The secondary proton energy threshold of approximately 50 MeV is consistent with the threshold for primary protons in charged-current interactions [39]. However, due to the lack of hits from other particles in the same location, these isolated charge depositions can be reconstructed at significantly lower energies in principle. Further work to lower the proton threshold, including
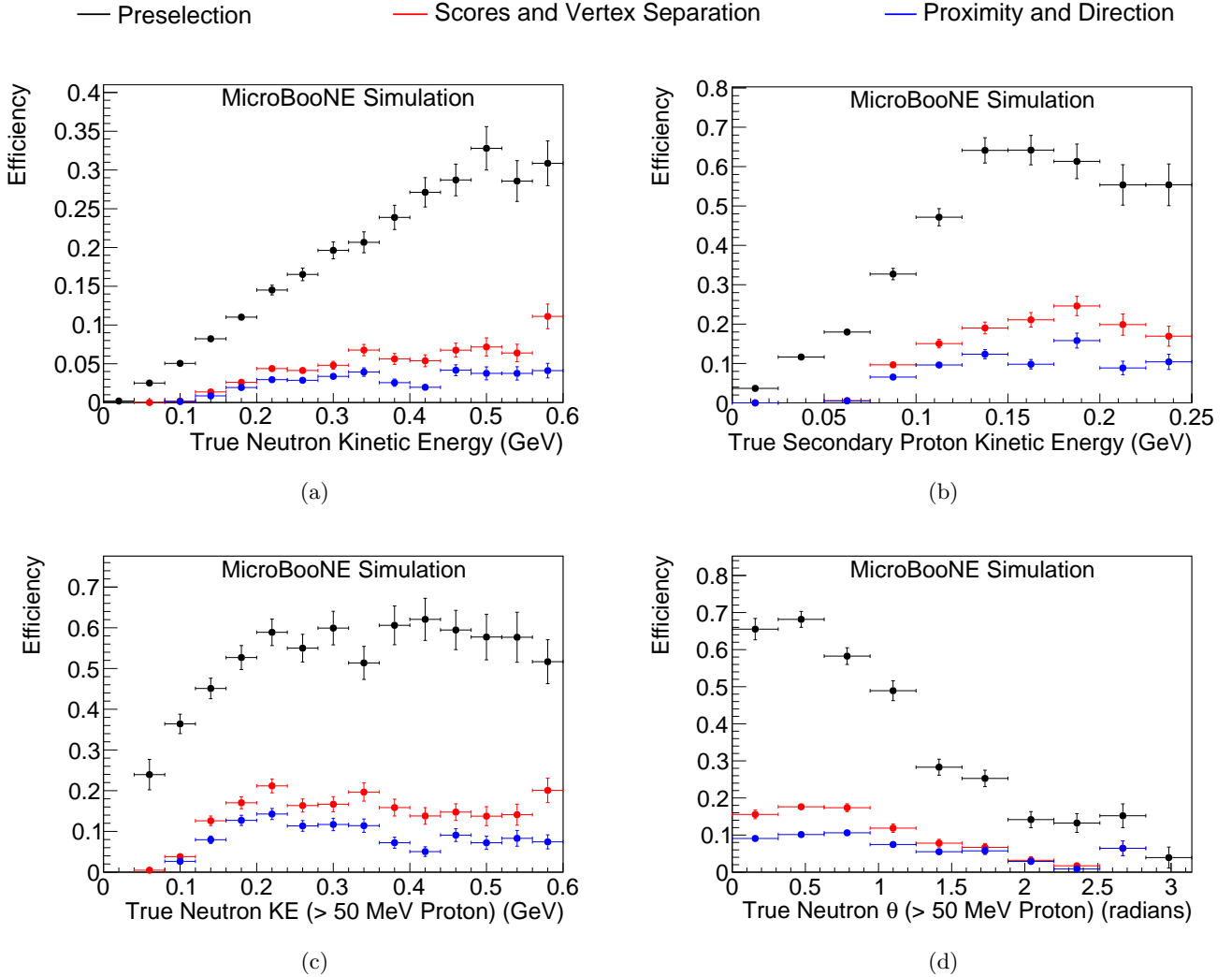
FIG. 10: (a) Neutron detection efficiency as a function of true neutron kinetic energy. (b) Secondary proton detection efficiency. (c) Neutron detection efficiency as a function of true neutron energy for neutrons that produce protons with kinetic energy 50 MeV or more. (d) Neutron detection efficiency as a function of neutron polar scattering angle for neutrons that produce protons with kinetic energy 50 MeV or more.

leveraging newly developed low-threshold reconstruction capabilities [29, 30], would lead to significant efficiency gains. Additionally, the selection could be expanded to consider protons not reconstructed as part of the neutrino slice – around 60% of neutron-induced protons in our sample.

V. SUMMARY AND CONCLUSIONS

We have demonstrated the ability to identify neutrons produced in neutrino interactions through the production of secondary protons from neutron interactions separated from the neutrino vertex. The sample of neutron candidates identified is 60% pure, with 48% purity when only considering primary neutrons. While the integrated effi-

ciency remains low, there remain prospects for improvement. Additionally, the efficiency is lowest for low-energy neutrons which contribute less to neutrino energy biases, and highest for neutrons above 250 MeV kinetic energy, which could represent significant biases to neutrino energy estimates.

The methods outlined in this paper would be applicable to any LArTPC and allow for the measurement of neutrino-induced neutron production in MicroBooNE, the SBN experiments, or DUNE in the future. Additionally, this method can be used to provide statistical separation of neutrino and antineutrino events in a non-magnetized LArTPC, and statistical separation of a sample of events known to have biased neutrino energy estimators which may reduce uncertainties in an oscillation measurement.

ACKNOWLEDGMENTS

[1] B. Abi *et al.* (DUNE). "Deep Underground Neutrino Experiment (DUNE), Far Detector Technical Design Report, Volume I Introduction to DUNE." *JINST* **15** T08008, 2020. DOI: 10.1088/1748-0221/15/08/T08008

[2] K. Abe *et al.* (Hyper-Kamiokande). "Hyper-Kamiokande Design Report." [arXiv:1805.04163 [physics.ins-det]].

[3] P. Adamson *et al.* (MINOS+ Collaboration). "Precision Constraints for Three-Flavor Neutrino Oscillations from the Full MINOS+ and MINOS Dataset." *Phys. Rev. Lett.* **125** 131802, 2020. DOI:10.1103/PhysRevLett.125.131802

[4] M. A. Acero *et al.* (NOνA Collaboration). "Improved measurement of neutrino oscillation parameters by the NOνA experiment." *Phys. Rev. D.* **106** 032004, 2022. DOI: 10.1103/PhysRevD.106.032004

[5] P. Abratenko *et al.* (MicroBooNE Collaboration). "First Constraints on Light Sterile Neutrino Oscillations from Combined Appearance and Disappearance Searches with the MicroBooNE Detector." *Phys. Rev. Lett.* **130** 011801, 2023. DOI: 10.1103/PhysRevLett.130.011801

[6] A. P. Furmanski and J. T. Sobczyk. "Neutrino energy reconstruction from one muon and one proton events." *Phys. Rev. C.* **95** 065501, 2017. DOI: 10.1103/PhysRevC.95.065501

[7] A. P. Furmanski and C. Hilgenberg. "Neutrino Energy Estimation in Neutral Current Interactions and Prospects for Sterile Neutrino Searches." *Phys. Rev. D.* **103** 112011, 2021. DOI: 10.1103/PhysRevD.103.112011

[8] J. Liu *et al.* "Deep-Learning-Based Kinematic Reconstruction for DUNE." [arXiv:2012.06181 [physics.ins-det]].

[9] M. Ascencio-Sosa *et al.* (ANNIE Collaboration). "Deployment of Water-based Liquid Scintillator in the Accelerator Neutrino Neutron Interaction Experiment" [arXiv:2312.09335 [hep-ex]].

[10] M. Shinoki *et al.* (Super-Kamiokande Collaboration). "Measurement of the cosmogenic neutron yield in Super-Kamiokande with gadolinium loaded water" *Phys. Rev. D.* **107** 092009, 2023. DOI: 10.1103/PhysRevD.107.092009

[11] P. An *et al.* "Measurement of ^{nat}Pb(ν_e, Xn) production with a stopped-pion neutrino source" *Phys. Rev. D.* **108** 072001, 2023. DOI: 10.1103/PhysRevD.108.072001

[12] A. Olivier *et al.* (MINERνA Collaboration). "Measurement of the multineutron $\bar{\nu}_\mu$ charged current differential cross section at low available energy on hydrocarbon" *Phys. Rev. D.* **108** 112010, 2023. DOI: 10.1103/PhysRevD.108.112010

[13] M. Elkins *et al.* (MINERνA Collaboration). "Neutron measurements from antineutrino hydrocarbon reactions" *Phys. Rev. D.* **100** 052002, 2019. DOI: 10.1103/PhysRevD.100.052002

[14] R. Acciarri *et al.* (ArgoNeuT Collaboration). "Demonstration of MeV-scale physics in liquid argon time projection chambers using ArgoNeuT." *Phys. Rev. D* **99**, 012002, 2019. DOI: 10.1103/physrevd.99.012002.

[15] R. Acciarri *et al.* "Design and construction of the MicroBooNE detector" *JINST* **12** P02017, 2017 DOI: 10.1088/1748-0221/12/02/P02017

[16] A. A. Aguilar-Arevalo *et al.* (MiniBooNE Collaboration). "Neutrino Flux Prediction at MiniBooNE." *Phys. Rev. D* **79**, 072002, 2009. DOI: 10.1103/PhysRevD.79.072002.

[17] P. Abratenko *et. al.* (MicroBooNE Collaboration). "Measurement of space charge effects in the MicroBooNE LArTPC using cosmic muons." *JINST* **15** P12037, 2020. DOI: 10.1088/1748-0221/15/12/p12037

[18] P. Abratenko *et. al.* (MicroBooNE Collaboration). "Measurement of the atmospheric muon rate with the MicroBooNE Liquid Argon TPC." *JINST* **16** P04004, 2021. DOI: 10.1088/1748-0221/16/04/P04004

[19] D. Kaleko. "PMT triggering and readout for the MicroBooNE experiment." *JINST* **8** C09009, 2013. DOI: 10.1088/1748-0221/8/09/C09009.

[20] C. Andreopoulos *et al.* . "The GENIE neutrino Monte Carlo generator." *Nucl. Instr. and Meth. A* **614** 1, 2010. DOI: 10.1016/j.nima.2009.12.009.

[21] L. Alvarez-Ruso *et al.* . "Recent highlights from GENIE v3." *Eur. Phys. J. Spec. Top.* **230**, 2021. DOI: 10.1140/epjs/s11734-021-00295-7.

[22] P. Abratenko *et. al.* (MicroBooNE collaboration). "New CC0π GENIE model tune for MicroBooNE." *Phys. Rev. D* **105** 072001, 2022. DOI: 10.1103/PhysRevD.105.072001

[23] S. Agostinelli *et al.*"Geant4—a simulation toolkit." *Nucl. Instr. and Meth. A* **506** 3, 2003. DOI: 10.1016/S0168-9002(03)01368-8.

[24] J. Allison *et al.*"Recent developments in Geant4." *Nucl. Instr. and Meth. A* **835**, 2016. DOI: 10.1016/j.nima.2016.06.125.

[25] E. L. Snider and G. Petrillo. "LArSoft: toolkit for simulation, reconstruction and analysis of liquid argon TPC neutrino detectors." *Journal of Physics: Conference Series* **898**, 2017. DOI: 10.1088/1742-6596/898/4/042057.

[26] S. Andringa *et al.* "Low-energy physics in neutrino LArTPCs" *J. Phys. G: Nucl. Part. Phys.* **50**, 033001, 2023. DOI: 10.1088/1361-6471/acad17

[27] S. Martynenko *et al.* (CAPTAIN Collaboration). "Measurement of the neutron cross section on argon between 95 and 720 MeV." *Phys. Rev. D* **107**, 072009, 2023. DOI: 10.1103/PhysRevD.107.072009

[28] D. O. Rivera. "Neutron Cross Section Measurement In The ProtoDUNE-SP Experiment." (FERMILAB-THESIS-2021-31) [Doctoral Dissertation, University of Pennsylvania].

[29] P. Abratenko *et. al.* (MicroBooNE collaboration). "Observation of radon mitigation in MicroBooNE by a liquid argon filtration system." *JINST* **17** 11, 2022. DOI: 10.1088/1748-0221/17/11/P11022.

[30] P. Abratenko *et. al.* (MicroBooNE collaboration). "Measurement of ambient radon progeny decay rates and energy spectra in liquid argon using the MicroBooNE detector" *Phys. Rev. D* **109**, 052007, 2024 DOI:10.1103/PhysRevD.109.052007

[31] A. Friedland and S. Li. "Understanding the energy resolution of liquid argon neutrino detectors" *Phys. Rev. D* **99**, 036009, 2019 DOI: 10.1103/PhysRevD.99.036009

[32] A. Friedland and S. Li. "Simulating hadron test beams in liquid argon" *Phys. Rev. D* **102**, 096005, 2020 DOI: 10.1103/PhysRevD.102.096005

[33] R. Acciarri *et al.* (MicroBooNE Collaboration). "The Pandora multi-algorithm approach to automated pattern recognition of cosmic-ray muon and neutrino events in the MicroBooNE detector." *Eur. Phys. J. C* **78** 82, 2018. DOI: 10.1140/epjc/s10052-017-5481-6.

[34] S. Gardiner. "Double-differential Measurements of Mesonless Charged-Current Muon Neutrino Interactions on Argon with Final-State Protons using the MicroBooNE Detector." DOI: 10.48550/arXiv.2403.19574

[35] C. Adams *et. al.* (MicroBooNE collaboration). "Calibration of the charge and energy loss per unit length of the MicroBooNE liquid argon time projection chamber using muons and protons." *JINST* **15** P03022, 2020. DOI: 10.1088/1748-0221/15/03/P03022.

[36] P. Abratenko *et. al.* (MicroBooNE collaboration). "Calorimetric classification of track-like signatures in liquid argon TPCs using MicroBooNE data." *J. High Energ. Phys.* **2012** 153, 2021. DOI: 10.1007/JHEP12(2021)153

[37] P. Abratenko *et al.* (MicroBooNE Collaboration). "Multidifferential cross section measurements of ν_μ-argon quasielasticlike reactions with the MicroBooNE detector." *Phys. Rev. D* **108** 053002, 2023. DOI: 10.1103/PhysRevD.108.053002.

[38] P. Abratenko *et al.* (MicroBooNE Collaboration). "Search for an anomalous excess of inclusive charged-current ν_e interactions in the MicroBooNE experiment using Wire-Cell reconstruction." *Phys. Rev. D* **105** 112005, 2022. DOI: 10.1103/PhysRevD.105.112005

[39] P. Abratenko *et. al.* (MicroBooNE Collaboration). "Measurement of differential cross sections for ν_μ-Ar charged-current interactions with protons and no pions in the final state with the MicroBooNE detector." *Phys. Rev. D* **102** 112013, 2020. DOI: 10.1103/PhysRevD.102.112013